Electrohydrodynamic instability of premixed flames under manipulations of dc electric fields

Yihua Ren, Wei Cui, and Shuiqing Li[*]

Key laboratory for Thermal Science and Power Engineering of Ministry of Education,
Department of Energy and Power Engineering, Tsinghua University, Beijing, 100084, China

We report an electrohydrodynamic instability in a premixed stagnation flame under manipulations of a dc electric field. This instability occurs when the electric field strength is at a certain value below the breakdown threshold, which is 0.75 kV/cm in the experimental setup. Above this value the flame front suddenly transits from a substrate-stabilized near-flat shape to a nozzle-stabilized conical surface, accompanied by a jump in the electric current through the flame field. At the transition moment, the flame spontaneously propagates upstream to the nozzle while the flow velocity at the upstream of the flame front decreases to zero, as revealed by high-speed photographs and PIV measurements. These phenomena indicate a transient balance between the fluid inertia and the electric body force around the instability threshold. A quantitative model suggests that the flame instability can be explained by a positive feedback loop, where the electric field applies a nonuniform electric body force, pulling the flame front upstream, and the pulled flame front in turn enhances the local electric body force. The electrohydrodynamic instability occurs when the electric pulling is strong enough and both the growth rates and the magnitudes of the electric body force on flame exceed those of the fluid dynamic pressure.

DOI: 10.1103/PhysRevE.97.013103

I. INTRODUCTION

Manipulating flames by electric fields has been investigated for decades in various ways like driving convection [1–4], stabilizing flame near limit conditions [5,6], altering flame shapes [7,8], extinguishing fires [9], controlling flame-synthesized nanoparticles [10–13], removing pollutant like soot [14,15], NOx [16], and CO [17]. Generally speaking, electric fields have three main effects on flames [18]: (i) an electrohydrodynamic effect caused by electric body forces [19,20], (ii) a chemical kinetic effect due to reactions enhanced by ions or electrons [21], and (iii) a thermal heating effect [22]. Despite many debates, it is believed that the electrohydrodynamic effect is predominantly responsible for the flame changes under weak subbreakdown electric fields. In detail, ions and electrons (dominated by CHO^+, H_3O^+, electrons, O_2^-, with a characteristic density of $\sim 10^{10-11}$ cm^{-3} [23]) generated in flames collide with neutral molecules, which, in a macroscopic view, exert a net body force on the fluids.

Previous studies on the electrohydrodynamic effects mainly focused on the hydrodynamic response of flames under the manipulations of electric fields. For instance, steady or slowly varied electric fields can significantly induce gas convection, i.e., the so-called ionic winds [1,2,4,20,24]. The convection flows can substitute gravity [2], crush down flame shape [4], and extend the flame stabilization zone [25]. Analyses in these studies concentrated on the one-way action of electric fields on flames. However, the reverse impact of the flame front on its electric responses, though recognized in several experiments and simulations, is still not well addressed. In our recent work [26], it was found that a nonuniform electric body force localizes at the corner position of an envelope flame front, which then significantly perturbs the flame. A similar phenomenon of nonuniform current density was also discovered in the simulation of a jet diffusion flame by Belhi *et al.* [27]. Therefore, the curved flame fronts can directly influence the current density distributions and generate the nonuniform electric body forces. Furthermore, the nonuniform forces can in turn affect the flow fields and manipulate the flame fronts. As a result, the two-way interactions between the hydrodynamic and electric responses of flames may form a positive feedback loop, that is, an electrohydrodynamic instability. Due to the complex flame-electric field coupling, this flame instability is completely different from those under the influence of external forces as reported previous studies [7,28,29] and needs to be uncovered.

The object of this work is to demonstrate the electrohydrodynamic instability of flames under external subbreakdown electric fields. To achieve this, we utilize a premixed stagnation flame and observe its behavior under a uniform dc electric field. Flame chemiluminescence, electric characteristics of the flame, and the flow patterns are examined at different external voltages. A quantitative model is proposed to demonstrate spatial distributions of the electric potential, the current density, and the electric body force under a predefined flame field. Dynamic characteristics of the electrohydrodynamic instability phenomenon are further recorded by a high-speed camera. Two necessary conditions for the instability are identified, based on which corresponding methods are proposed to avoid it.

II. EXPERIMENT

The experimental assembly of the stagnation flame and the static electric field is shown in Fig. 1. Premixed gases CH_4, O_2, and N_2 (molar composition 0.07:0.20:0.73) flowed through a
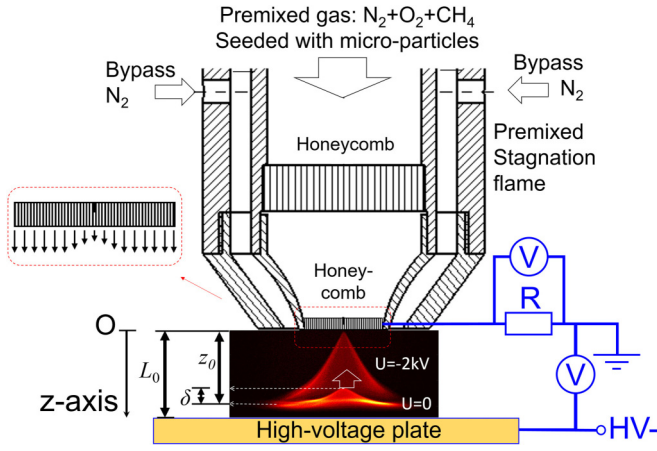
*lishuiqing@tsinghua.edu.cn

FIG. 1. Schematic of the stagnation flame setup, the electric circuit system, and cameras (a Nikon camera for static images and a high-speed camera for dynamic images). The premixed gas flows through the honeycomb nozzle and the flame is stabilized on the stagnation plate or the nozzle outlet. The negative high voltage is added on the plate while the honeycomb nozzle is grounded. The pseudocolor image in the schematic indicates the chemiluminescence of CH*.

contoured nozzle at a velocity of 1 m/s. A specially designed honeycomb, placed at the outlet of the nozzle, allowed gas to flow through and generated a nonuniform axial velocity distribution at the inlet of the flame field. The axis velocity is lowest at the center, inducing the wrinkled flame front. The flow field was measured by a particle image velocimetry (PIV) system. In the PIV measurement, 2- to 4-μm alumina particles were seeded into the stagnation flow field. The trace particles are enlightened by a 2-W 450-nm continuous wave (CW) laser sheet and imaged by a Phantom V331 high-speed camera with a frame rate of 2000 fps and an exposure time of 489 μs.

Luminescence of chemically excited CH radicals ($A^2\Delta$) at the wavelength of 431 nm was used to demonstrate the flame front structure and the chemi-ionization layer, as the reaction CH* + O $\rightarrow$ CHO$^+$ + e^- dominates the charge generation in methane-air flames [23]. Hence, the flame was first filtered by a bandpass filter (centered at 430 nm with a full width at half maximum of 10 nm) before imaged by a Nikon D300s camera with an AF-S NIKKOR 100-mm f/3.2 lens. Two typical images of flame chemiluminescence are illustrated in Fig. 1. Dynamic behaviors of the flame front were recorded by a Phantom V311 high-speed camera with a frame rate of 1000 fps and exposure time of 990 μs.

A negative high-voltage power, controlled by a signal generator (RIGOL DG-4162), applied a sinusoidal electric field between the honeycomb at the nozzle outlet and the substrate. The sinusoidal voltage has a period $\sim 10^2$ s, which is long enough to be regarded as a dc voltage. According to an electrostatic simulation, the electric field in absence of the flame is uniform in space especially at the center zone of the flow field. A resistor of 100 $k\Omega$ was added in the electric circuit to prevent breakdown and protect the power. The magnitude of the applied voltages U and the electric currents I that flowed through the circuit were monitored.

III. SIMULATION

To analyze the electric response of a given flame front, we must consider the charge transport behaviors in the flame field. Referring to previous one-dimensional simulations [1,30], a two-dimensional model is established to describe the migration, diffusion, and reaction of charges in the predefined axisymmetric flame field:

$$\nabla \cdot (-D_k \nabla n_k) + \nabla \cdot [\mu_k Z_k n_k (-\nabla V)] = R_k, \tag{1a}$$

$$\nabla \cdot \nabla V = -\frac{e}{\epsilon_0} \sum_k n_k Z_k. \tag{1b}$$

Here, D_k, Z_k, and μ_k are the diffusion coefficients, sign of charges, and mobility of species k, respectively; the subscripts k includes positive ions (p), electrons (e), and negative ions (m); V is the electric potential distribution; e is the elementary charge; and ϵ_0 is the vacuum permittivity. In this model, the convection of charged species is ignored because the ion drift velocity at 100 V/cm is on the order of 1 m/s, which is approximately 10 times larger than the flow velocity $\approx$ 0.1 m/s. This approximation has also been utilized in previous works [1,30]. The diffusion and mobility of charged species are correlated by the Einstein relation, $D_k = \mu_k k_B T / e$ [31]. R_k stands for the reaction term of different species:

$$R_p = k_i g_i(z,r) - k_r n_p n_e, \tag{2a}$$

$$R_e = k_i g_i(z,r) - k_r n_p n_e - k_a g_a(z,r) n_e, \tag{2b}$$

$$R_m = k_a g_a(z,r) n_e, \tag{2c}$$

where k_i, k_r, k_a are the chemi-ionization, recombination, and attachment rates, respectively. Referring to the reaction layer assumption in the previous one-dimensional models [1,30], the normalized spatial distributions functions $g_i(z,r)$ and $g_a(z,r)$ in our two-dimensional model are used to represent the chemi-ionization and attachment distributions based on the prescribed flame surface structure from measurement.

In detail, the chemi-ionization is assumed to be induced exclusively by the reaction CH + O $\rightarrow$ CHO$^+$ + e^- [31–33]. The attachment is dominated by the reactions e^- + O$_2$ + O$_2$ $\rightarrow$ O$_2^-$ + O$_2$ and e^- + O$_2$ + N$_2$ $\rightarrow$ O$_2^-$ + N$_2$ [31]. The global recombination coefficient is given by 1.14×10^{17} cm^3/(mol s) [27]. Since the flame stretch effect is negligible in the fuel-lean CH$_4$-air premixed gases due to the near-unity Lewis number [34], the premixed flame structure of the curved flame surface along its normal direction can be modelled locally as a one-dimensional flame. In addition, the neutral species can be regarded as a bath gas for ions and electrons and not influenced by the reactions of charges due to their low concentrations [31]. Therefore, the concentrations of neutral species and the temperatures along the flame front can be directly obtained from a one-dimensional CHEMKIN simulation based on the neutral species reactions. According to the local temperatures and concentrations of CH and O, we can then calculate the profile of the chemi-ionization reaction rate and fit it by a Gaussian distribution $k_i g_i(x)$. The normalized profile $g_i(x)$ can be converted into the two-dimensional spatial distribution $g_i(z,r)$ by letting the spatial variable x be the distance between a point (z,r) to its nearest position of the flame surface. Here the flame surface is extracted from the measured

TABLE I. Boundary conditions of the simulation where Γ is the flux of species k at z or r directions.

	Nozzle, $z = 0$	Substrate, $z = L$	Centerline, $r = 0$	Outlet, $r = R$
Species	$\Gamma_{k,z}(0,r) = \min(-\frac{\partial V}{\partial z}\mu_k Z_k e n_k, 0)$	$\Gamma_{k,z}(L,r) = \max(-\frac{\partial V}{\partial z}\mu_k Z_k e n_k, 0)$	$\partial\Gamma_{k,r}(z,0)/\partial r = 0$	$\partial\Gamma_{k,r}(z,R)/\partial r = 0$
Electric field	$V(0,r) = 0$	$V(L,r) = V_0$	$\partial V(z,0)/\partial r = 0$	$\partial V(z,R)/\partial r = 0$

chemiluminescence image. Similarly, the attachment coefficient is calculated based on the local premixed flame front structure, fitted by an error function $k_a g_a(x)$, and, finally, converted into $k_a g_a(z,r)$. The reaction rates, spatial distribution functions, and other coefficients in the simulation are detailed in the Appendix.

The boundary conditions are shown in Table I. The species flux at the electrode is determined by the migration under the local electric field. The equations are solved by a successive over relaxation method. A first-order upwind discretization is used on uniform rectangular grids points. Grid convergence is verified with three consecutively refined meshes from 2000 (50×40) to 32 000 (200×160), and 8000 (100×80) meshes is selected. Finally, the current density and the electric body force can be obtained based on the distribution of charged species. Under the voltage of 1200 kV, the calculated current 0.39 μA is close to the measured value 0.32 ± 0.01 μA, which validates the model.

IV. RESULTS AND DISCUSSION

A. Steady features

As mentioned previously, adding electric fields on flames can drive the movement of positive charges (dominated by CHO^+ and H_3O^+) and negative charge (dominated by electrons) in flames. The movement causes electric and hydrodynamic responses of flames simultaneously. Steady features of these responses are demonstrated in this section.

Figure 2 shows the current responses of the stagnation flame together with the flame chemiluminescence images at different applied voltages. When the applied voltages are smaller than 0.3 kV, the current is approximately proportional to the applied voltage, as shown in the double logarithmic plot of the $I-U$ curve at the inset of Fig. 2(a). This proportionality holds as the net charge density is too small to influence the external electric field. In the linear regime, recombination of charges rivals the ion generation. When the voltages are larger than 0.3 kV, the linear relation breaks down and the $I-U$ curve
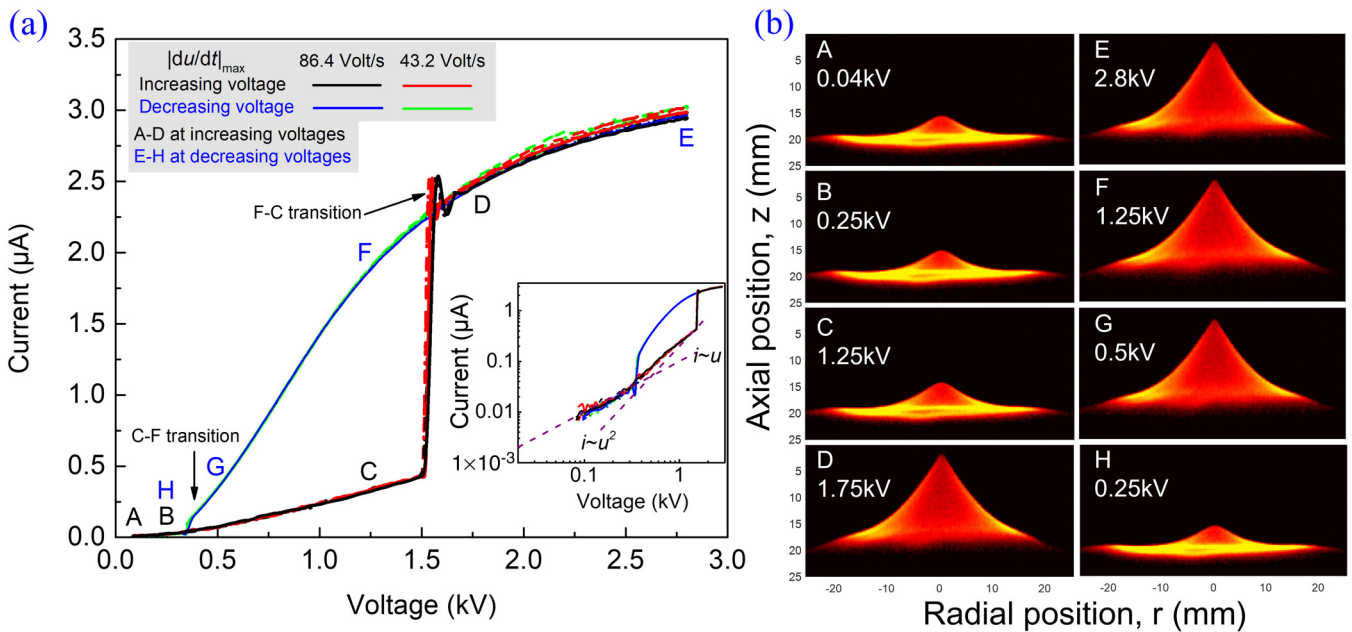

FIG. 2. (a) Electric current as a function of the applied voltage. Solid, dashed, and dotted lines stand for the first, second, and third cycles of changing voltages, respectively. The black (the dark line following points A-B-C-D-E) and blue (the dark gray line following points E-F-G-H) lines indicate the increasing and decreasing lines when the periodic time of applied voltages is 100 s, i.e., the maximum $|dU/dt|$ is 86.4 V/s; the red (the light gray line following points A-B-C-D-E) and green (the light gray line following points E-F-G-H) lines indicate the increasing and decreasing lines when the periodic time is 200 s, i.e., the maximum $|dU/dt|$ is 43.2 V/s. The consistence of these lines indicates that the F-C and C-F transitions are repeatable and do not depend on the increasing rate of the applied voltages. The inlet figure shows the double logarithm curves of the same $I-U$ curve; the purple dashed line indicates the fitting proportional and quadratic line. (b) Flame chemiluminescence at different voltages corresponding to the points A to H at the upper $I-U$ curves. The pseudocolor images indicate the intensities of the flame chemiluminescence.
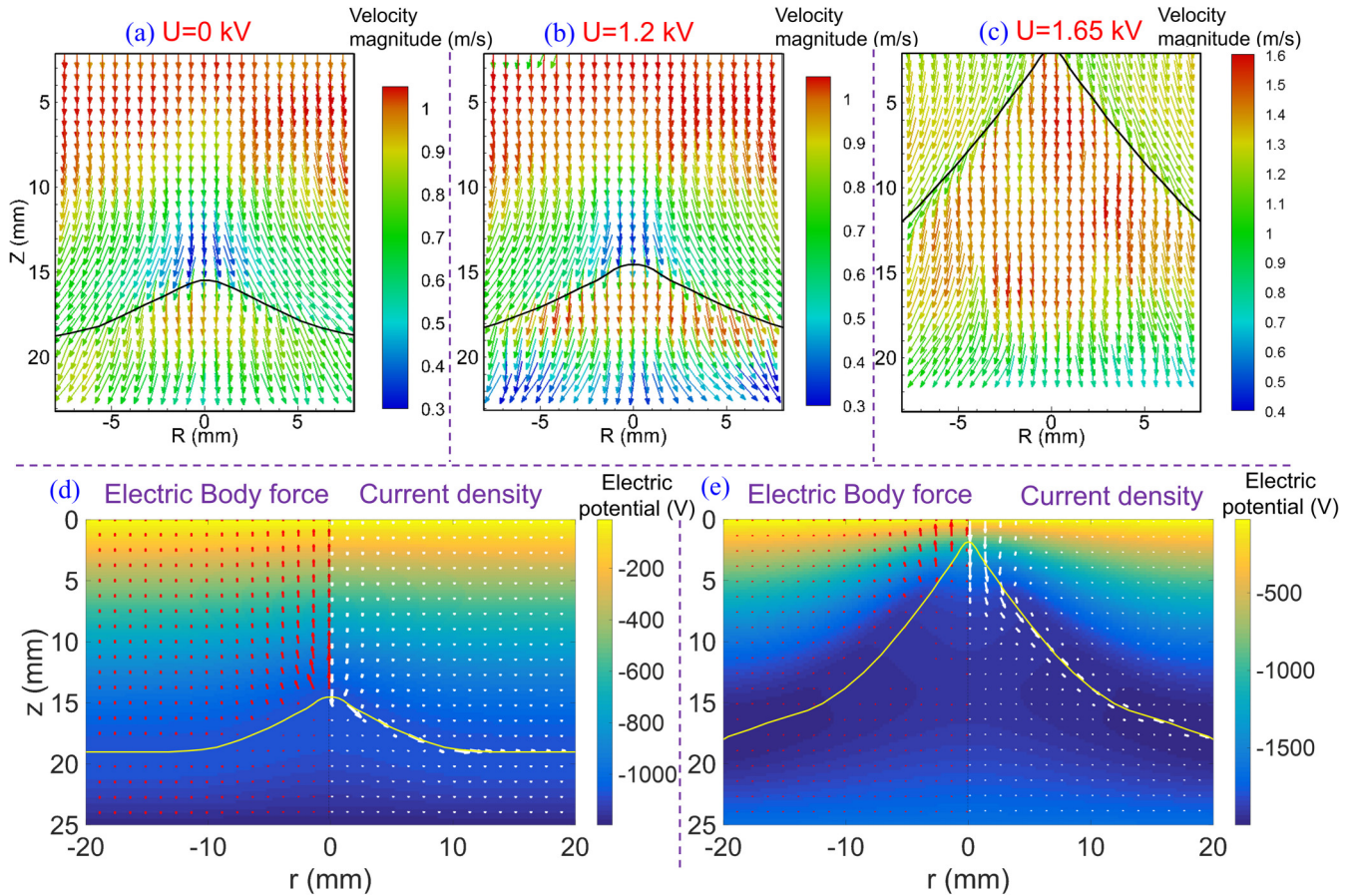
FIG. 3. PIV measured flow field at $U = 0$ (a), 1.2 kV (b), and 1.65 kV (c). Electric body forces [red (dark gray) arrows in the left half], current densities (white arrows in the right half), and the electric potentials at $U = 1.2$ kV (d) and 1.65 kV (e). Lengths of the arrows are proportional to magnitudes of the vectors. The maximum electric body force is 19.3 N/m^3 at $U = 1.2$ kV and 770.2 N/m^3 at $U = 1.65$ kV; the maximum current density is 0.012 A/m^2 at $U = 1.2$ kV and 0.67 A/m^2 at $U = 1.65$ kV. The flame fronts obtained from the chemiluminescence are plotted by black and white lines.

approaches a quadratic function, indicating a space-charge regime. In this regime, the net charge density is approximately proportional to the applied field strength, i.e., $n_c \propto E$, and the current density then scales as $j \propto e n_c E \mu \propto E^2$ (where μ is the mobility). For the above two regimes, the current responses are well consistent with previous theoretical and simulation studies [20,30], as the flame surfaces keep almost unchanged [as illustrated in the flame images A–C of Fig. 2(b)], which complies with basic assumptions in these studies.

However, when the voltage further increases, the classical theory does not hold any longer. The current jumps at a critical voltage about 1.5 kV, accompanied by a flame transition from a near-flat structure to a conical one. A video of the flame transition together with the corresponding $I−U$ curve is presented in the Supplemental Material [35]. The flame images (D–G) in Fig. 2(b) indicate that the conic flame is stable and does not depend on the voltages. The current responses of the flame almost lie in another $I−U$ curve completely different from the previous one. In this curve, the flame current plateaus with further increasing voltages, indicating the approaching of a saturation regime [20]. When the voltage decreases to another transition point, the flame transits back from the conical to the near-flat structure when the current falls back to the original one. It is noteworthy that the flat-to-conical (F–C)

and conical-to-flat (C–F) transition points do not coincide with each other. This hysteresis phenomenon, which has been widely observed in state transitions [36,37], implies a nonlinear dynamic system.

To better explain the F–C transition, flow fields of the flame at different voltages were measured by PIV, as shown in Figs. 3(a)–3(c). In absence of the electric field, the velocity jumps across the flame front due to the thermal expansion effect, and then approaches an axisymmetric divergence flow pattern before reaching the substrate. Velocities at $U = 1.2$ kV are similar with that at $U = 0$. Specifically, both flow fields have low-velocity zones in the central region at upstream of the flame front. The major difference is that under the electric field, the low-velocity zone moves slightly to the nozzle accompanied with the flame front. Moreover, it should be noted that the velocity magnitudes at the low-velocity zone, which is equivalent to the local flame speed, keep almost constant under different voltages. Therefore, the subbreakdown electric field manipulates the flame front by altering the upstream flow field other than directly changing the flame speed, which is consistent with previous studies [38,39]. Besides, as shown in Fig. 3(d), simulation of the charge transport behaviors based on the measured flame front reveals that the current density follows the conductive flame front and generates a large electric
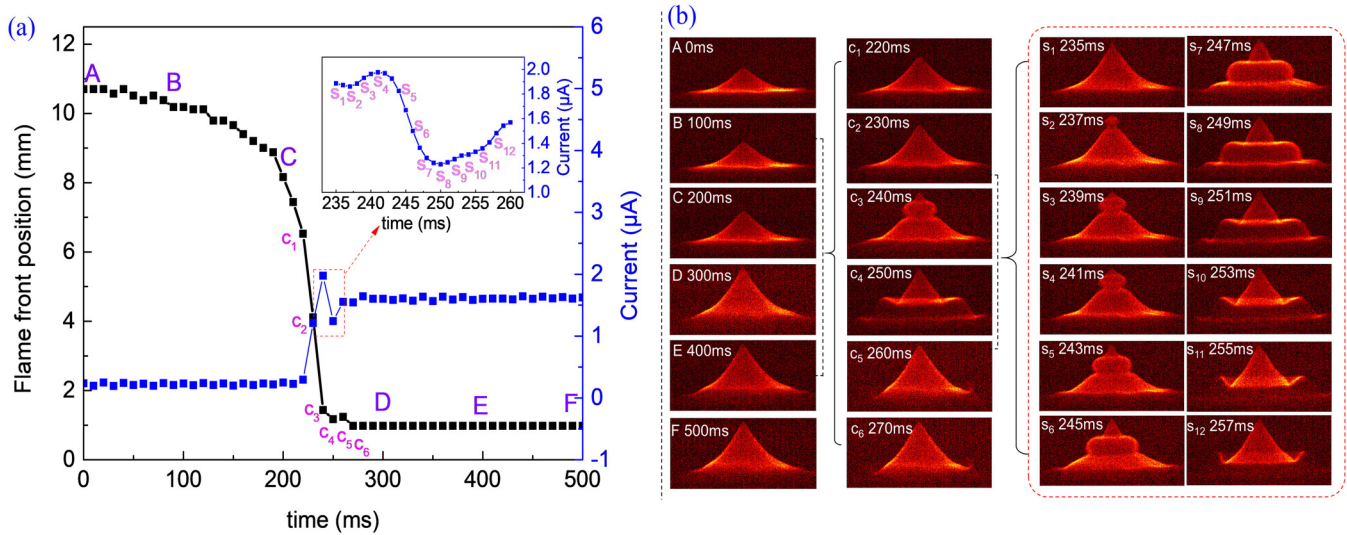
FIG. 4. Transition process of flame structure. (a) Position of the flame front in the center (black squares and line) and the current response [blue (dark gray) squares and line] during a typical F–C transition. The current responses from 235 to 257 ms are zoomed in at the inset figure. (b) Flame front structure imaged by a high-speed camera.

body force about 19.3 N/m^3 localized at the upstream of the flame wrinkle.

After the F–C transition, the flow field significantly changes due to the flame front transition. According to the classical combustion theory, the velocity component perpendicular to the flame front increases to $(\rho_u/\rho_b)s_L$ while the velocity component tangential to the front keeps constant. The heavily inclined flame front gives rise to large tangential velocities, which finally results in the large velocity magnitudes at downstream of the flame front, as shown in Fig. 3(c). Similarly to the electric responses of the near-flat flame front, the electric current flows along the inclined flame front. However, the maximum electric body force in this mode reaches as high as 770 N/m^3, almost 40 times higher than that at the flat mode, which is large enough to reduce the upstream flow velocity to the flame speed. Therefore, effects of electric fields on flames strongly depend on the original flame structures, which can well explain the bifurcated flame stabilization modes for increasing and decreasing voltages.

B. Dynamic features

Dynamic behaviors of the flame transition between the two stabilization modes are further investigated by tracking the flame front transition. Figure 4 illustrates variations of the flame front and the corresponding current responses within 0.5 s in one typical F–C transition. The flame stabilizes in the near-flat mode from 0 ms to ∼220 ms and in the conical mode after ∼260 ms, while the currents keep almost constant in each mode. As shown in the flame snapshots of c_1–c_3, the flame wrinkle inclines and develops into the conical structure during the transition within 40 ms, while the current rapidly increase simultaneously. The snapshots s_1–s_{12} demonstrate that the flame front is fiercely perturbed before reaching the conical stabilization mode. The current strongly oscillates accompanied by the unsteady flame front, as seen in the inset of Fig. 4(a). The synchronization between currents and flame

fronts validates the strong dependency of the electric responses on the flame front.

We noted that the position of the flame front in the center transits from 6.527 mm (c_1) to 1.436 mm at (c_3) within 20 ms, which corresponds to a transition speed of 0.255 m/s. The flame speed is calculated to be 0.259 m/s by CHEMKIN and measured to be 0.3 ± 0.07 m/s by the PIV result. The flame speed is defined as the propagation velocity of a flame front in a quiescent mixture of unburned gases, which is equal to the unburned flow velocity of a stationary flame front [34]. Consistence between the flame speed and the transition speed indicates that the F–C transition is a flame propagation process when the upstream unburned gas velocity is reduced to zero by the electric body force.

More importantly, since the applied voltage increases less than 1.6 V within 40 ms from c_1 to c_3, the transition can be regarded as a spontaneous process and must be triggered by a positive feedback mechanism. When the flame front gradually inclines and moves upstream, both the fluid inertia and the electric body force increase. As the two factors drive the flame front movement in reverse directions, the critical point for triggering the spontaneous process is that growth rates of the electric body force exceed that of the fluid inertia. If this condition can be satisfied, then the electric body force is able to reduce the local flow velocity and to pull the flame upstream. The more the flame fronts incline, the larger the electric body forces are, which forms a positive feedback loop.

C. Electrohydrodynamic instability

The positive feedback loop originates from the nonuniform distributions of electric body forces. This nonuniformity is caused by the electrostatic screening effect of the flame front. Because the Debye length of the flame plasma, $\lambda = \sqrt{\epsilon_0 k_B T/(ne^2)} \sim 10^{-5}$ m, is much smaller than the flame thickness $l_F \sim 10^{-3}$ m, the flame front can be considered a quasineutral equipotential plane, as demonstrated in Figs. 3(d)
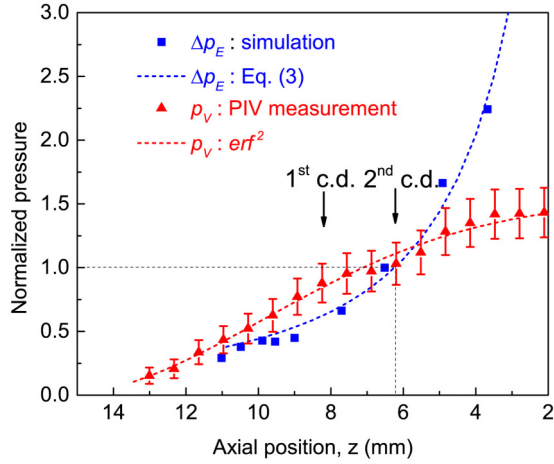
FIG. 5. Normalized electric pressure differences based on the simulated electric body forces (blue squares) and fluid dynamic pressure based on the PIV velocities (red triangles) at positions of the flame wrinkle during the F–C transition. The blue (dark gray) dotted line and red (light gray) dotted line represent the analytic results based on Eq. (3) and the square of an error function, respectively. The electric pressure difference and the fluid dynamic pressure are normalized by their respective pressures at the flashback point [namely the c_1 point with $z \approx 6$ mm in Fig. 4(a)]. Two arrays point to the two critical positions of the F–C transition, i.e., the first and secon necessary conditions for the electrohydrodynamic instability.

and 3(e). Under external electric fields, the charges tend to redistribute in the equipotential plane to minimize their electric potential energy until there is no potential difference among various parts of the plane. Outside the flame front, electric field strengths gradually increase, together with the generations of net charges in this region. Drews *et al.* [1] demonstrated this effect and proposed an expression for a characteristic electric pressure difference as $\Delta p_E = \frac{1}{2}\epsilon_0 E_0^2$ based on the one-dimensional reaction layer assumption. However, when the surface is not strictly perpendicular with the external electric field, the strongest electric field is generated between the electrode and the flame wrinkles at the smallest distance. If the flame wrinkle has a length scale of δ in the electric field directions, the local electric field can be approximately expressed by $E_z \approx E_0 z_0 / (z_0 - \delta)$. The electric pressure difference can be estimated by

$$\Delta p_E = \frac{1}{2}\epsilon_0 E_0^2 \frac{z_0^2}{(z_0 - \delta)^2}, \qquad (3)$$

where E_0 is the original electric field without flame wrinkle and z_0 is the distance between the unwrinkled flame front and the electrode. As a result, the flame wrinkle closer to the electrode bears a larger electric body force, which leads to the nonuniform hydrodynamic response of the flame.

The nonuniform responses can further trigger the electrohydrodynamic flame instability after satisfying two necessary conditions. First, as mentioned above, the growth rates of electric pressure difference need to be equal or larger than that of fluid inertia. To demonstrate this effect, we compare the growth rate of the two quantities during the flame F–C
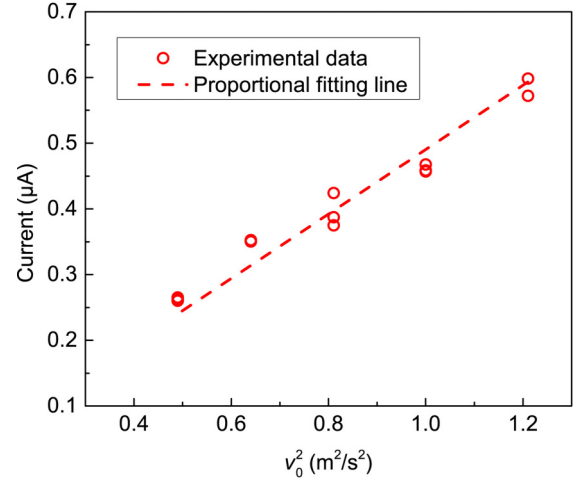

FIG. 6. Measured critical currents at the F–C transition point with different inlet flow velocities.

transition in our case. Based on the simulation, the electric body force distributions can be obtained with different flame structures at the same transition voltage. The electric body force along the centerline is then integrated into the electric pressure difference, i.e., $\Delta p_E = \int f_z dz$, where f_z is the axial electric body force from the simulation. The upstream fluid inertia can be evaluated by the fluid dynamic pressure $p_V = \rho_u v^2$ [40], where ρ_u is the unburned gas density and v is the unburned gas flow velocity excluding the electric body force effect. Here the gas flow velocity is estimated by the measured gas flow velocity profiles at $U = 0$ kV. As shown in Fig. 5, the electric pressure difference increases simultaneously with the fluid dynamic pressure as the flame front moves upstream. On one hand, the fluid dynamic pressure p_V obeys the square of the error function [41], as the impinging jet flow velocity can be fitted by an error function $v = v_0 \text{erf}\{\alpha[(L - z)/L - \delta/L]\}$, where α is a strain rate parameter, v_0 is the inlet velocity, and L_0, z, and δ are spatial parameters defined in Fig. 1. On the other hand, relation between the electric pressure difference Δp_E and the flame wrinkle position follows Eq. (3), namely a polynomial function with a degree of -2. It should be noted that the growth rate of the electric pressure difference continuously increases while that of the fluid dynamic pressure decreases. As a result, there exists a critical position where the growth rate of the electric pressure difference exceeds that of the fluid dynamic pressure.

After the first condition is satisfied, the electric pressure difference grows faster and finally exceeds the fluid dynamic pressure at the flame flashback position, which is the second necessary condition. To further validate it, we plot the measured currents near the F–C transitions with different inlet velocities, since the current density $\mathbf{j} = \sum e n_\pm \mu_\pm \mathbf{E}$ can approximately stand for the electric body force $\mathbf{f} = e(n_+ - n_-)\mathbf{E}$. As seen in Fig. 6, the critical currents are proportional to the square of the inlet flow velocities, which further confirms the second necessary condition.

Finally, the electrohydrodynamic instability of the flame occurs between two different stabilization modes. The near-flat substrate-stabilized mode is generated by the jet-impinging flow in absence of the electric field, while the conical nozzle-

stabilized mode is created by the electric body force near the nozzle electrode. Under the electric field, the original stagnation mode cannot stabilize the flame any longer after satisfying the above two conditions. Based on the above analyses, two solutions are proposed here to depress the instability and broaden the stabilization limit in other electric field– or plasma-assisted combustion systems. The first method is to increase distances between flames and electrodes (z_0 in our case). In this way, electric pressure differences Δp_E are less dependent on the nonuniformity of flame shapes (the flame wrinkle size δ in our case) according to Eq. (3). The second method, from the opposite perspective, is to directly stabilize flames by electrodes (in absence of electric fields) which can impede the flame transition to other potential modes after adding the electric field.

V. CONCLUSION

In summary, we report the electrohydrodynamic instability of the premixed stagnation flame under the subbreakdown dc electric field. When the applied voltage increases beyond 1.5 kV, the flame front suddenly transits from the near-flat substrate-stabilized mode to the conical nozzle-stabilized mode, accompanied by the current jump from the space-charge regime to the saturation regime. The electric body force is nonuniformly distributed at the upstream of the flame wrinkle, which expands the low-velocity zone and pulls the flame front upstream. A theoretical analysis of the Debye length of the flame plasma reveals that the nonuniformity of the electric body force originates from equipotentiality of the wrinkled flame front. Consequently, both the local electric field and the space charge density are largest at the flame wrinkle closest to the electrode. The electric responses of the flame, coupled with the hydrodynamic responses, further trigger the electrohydrodynamic instability of the flame front. High-speed camera and PIV measurements show that at the transition moment, the flow velocity decreases to zero and the flame front spontaneously flashbacks to the nozzle, indicating a transient balance between the electric pressure difference and the fluid inertia around the instability threshold. This flame transition phenomenon is driven by a positive feedback loop: the increased electric body force pulls the flame wrinkle upstream, which in turn enhances the local electric body force. Two necessary conditions are required to trigger the loop: (1) the growth rates of the electric pressure difference exceed than that of the fluid dynamic pressure, and (2) the electric pressure difference can balance or become larger than the fluid dynamic pressure to reduce unburned gas velocities to zero. Finally, two solutions are proposed to prevent the instability: (i) placing flames far from the electrode to weaken the dependence of the electric response

TABLE II. Reaction mechanism of the charged species.

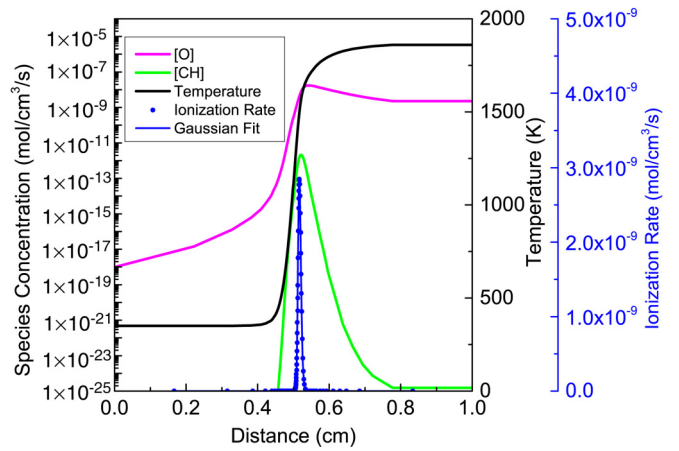|	A (cm³ mol s)	n	E_a (kJ/mol)
$CH + O \rightarrow CHO^+ + e^-$	2.51×10^{11}	0	7.12[a]
$e^- + O_2 + O_2 \rightarrow O_2^- + O_2$	1.52×10^{21}	-1	4.99[b]
$e^- + O_2 + N_2 \rightarrow O_2^- + N_2$	3.59×10^{21}	-2	0.58[b]

[a]Reference [27].
[b]Reference [31].

FIG. 7. Concentrations of CH, O, temperatures, and the chemionization rate of the reaction $CH + O \rightarrow CHO^+ + e^-$.

on the shapes of flame fronts and (ii) stabilizing flame by electrodes to isolate the flame in a single stabilization mode.

APPENDIX: COEFFICIENTS IN THE SIMULATION

The charge mobilities are $\mu_{p,m} = 2.9 \times 10^{-4}$ m²/(V s) for ions and $\mu_e = 0.4$ m²/(V s) for electrons according to previous works [9,30,42]. The diffusion coefficients are calculated
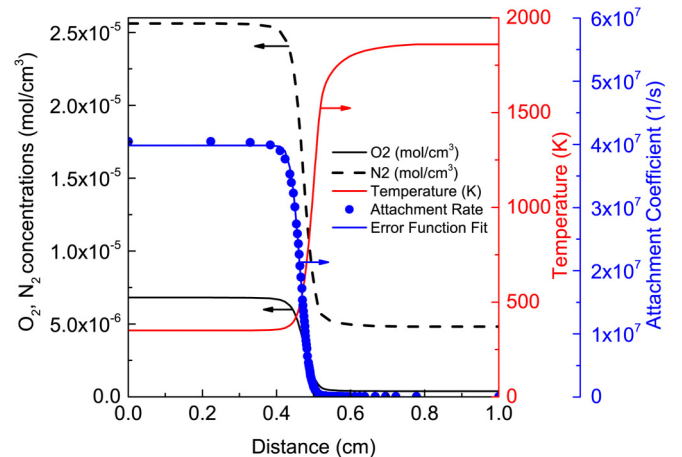

FIG. 8. Concentrations of O_2, N_2, temperatures, and the reaction coefficient of the attachment reactions $e^- + O_2 + O_2 \rightarrow O_2^- + O_2$ and $e^- + O_2 + N_2 \rightarrow O_2^- + N_2$.

based on the Einstein equation $D = \mu k_B T/e$. Following previous works [31–33,43], the chemi-ionization is assumed to occur exclusively by the reaction $CH + O \rightarrow CHO^+ + e^-$, and the reaction rate can be expressed by $AT^n \exp(-E_a/RT)$ with the coefficients A, n, and E_a shown in Table II. After obtaining the concentrations of CH and O and temperatures from a one-dimensional (1D) flame simulation by Chemkin, we can calculate the distribution of the chemi-ionization reaction rate and fit it by a Gauss distribution $k_i g_i(x)$, as shown in Fig. 7. For the 2D simulation, the normalized distribution $g_i(x)$ is converted into $g_i(z,r)$ by letting the spatial variable x be the distance between point (z,r) to the nearest position of the flame front.

Following Hu *et al.* [8] and Belhi *et al.* [27], the global recombination rate of electrons and positive ions (which is dominated by H_3O^+ in postflame regions) is given by 1.14×10^{17} cm^3/mol s. As for the attachment process, we utilized the reaction mechanism suggested by Prager *et al.* [31]. As shown in Fig. 8, the attachment coefficient can be obtained from O_2 and N_2 concentrations and temperatures according the reaction mechanism in Table II. The attachment is then fitted by an error function. The attachment coefficient is much larger at the upstream of the flame front than that at the downstream, agreeing well with the negative ions distributions in Gooding's experiment [43]. The error function is then normalized to $g_a(x)$ and converted into $g_a(z,r)$.

[1] A. M. Drews, L. Cademartiri, M. L. Chemama, M. P. Brenner, G. M. Whitesides, and K. J. M. Bishop, Phys. Rev. E **86**, 036314 (2012).

[2] F. B. Carleton and F. J. Weinberg, Nature **330**, 635 (1987).

[3] S. Karnani, D. Dunn-Rankin, F. Takahashi, Z.-G. Yuan, and D. Stocker, Combust. Sci. Technol. **184**, 1891 (2012).

[4] J. Schmidt and B. Ganguly, Combust. Flame **160**, 2820 (2013).

[5] M. Kim, S. Ryu, S. Won, and S. Chung, Combust. Flame **157**, 17 (2010).

[6] D. A. Lacoste, J. P. Moeck, D. Durox, C. O. Laux, and T. Schuller, J. Eng. Gas Turbines Power **135**, 101501 (2013).

[7] C. L. Maupin and H. H. Harris, Combust. Flame **97**, 435 (1994).

[8] J. Hu, B. Rivin, and E. Sher, Exp. Therm. Fluid Sci. **21**, 124 (2000).

[9] E. Sher, A. Pokryvailo, E. Jacobson, and M. Mond, Combust. Sci. Technol. **87**, 59 (1993).

[10] H. Zhao, X. Liu, and S. D. Tse, J. Nanopart. Res. **10**, 907 (2008).

[11] D. R. Hardesty and F. J. Weinberg, Proc. Combust. Inst. **14**, 907 (1973).

[12] Y. Wang, G. Sharma, C. Koh, V. Kumar, R. Chakrabarty, and P. Biswas, Aerosol Sci. Technol. **51**, 833 (2017).

[13] S. Li, Y. Ren, P. Biswas, and S. D. Tse, Prog. Energy Combust. Sci. **55**, 1 (2016).

[14] Y. Wang, G. Nathan, Z. Alwahabi, K. King, K. Ho, and Q. Yao, Combust. Flame **157**, 1308 (2010).

[15] M. Saito, T. Arai, and M. Arai, Combust. Flame **119**, 356 (1999).

[16] E. V. Vega, S. S. Shin, and K. Y. Lee, Fuel **86**, 512 (2007).

[17] A. Sakhrieh, G. Lins, F. Dinkelacker, T. Hammer, A. Leipertz, and D. Branston, Combust. Flame **143**, 313 (2005).

[18] Y. Ju and W. Sun, Prog. Energy Combust. Sci. **48**, 21 (2015).

[19] H. A. Wilson, Rev. Mod. Phys. **3**, 156 (1931).

[20] J. Lawton and F. J. Weinberg, Proc. R. Soc. London Ser. A-Math. Phys. Eng. Sci. **277**, 468 (1964).

[21] B. N. Ganguly, Plasma Phys. Control. Fusion **49**, B239 (2007).

[22] S. Marcum and B. Ganguly, Combust. Flame **143**, 27 (2005).

[23] A. Fialkov, Prog. Energy Combust. Sci. **23**, 399 (1997).

[24] D. A. Lacoste, Y. Xiong, J. P. Moeck, S. H. Chung, W. L. Roberts, and M. S. Cha, Proc. Combust. Inst. **36**, 4183 (2017).

[25] M. Kim, S. Chung, and H. Kim, Proc. Combust. Inst. **33**, 1137 (2011).

[26] Y. Ren, S. Li, W. Cui, Y. Zhang, and L. Ma, Combust. Flame **176**, 479 (2017).

[27] M. Belhi, P. Domingo, and P. Vervisch, Combust. Flame **157**, 2286 (2010).

[28] A. Jocher, H. Pitsch, T. Gomez, J. Bonnety, and G. Legros, Phys. Rev. E **95**, 063113 (2017).

[29] H. Gotoda, T. Miyano, and I. G. Shepherd, Phys. Rev. E **81**, 026211 (2010).

[30] Y. Xiong, D. G. Park, B. J. Lee, S. H. Chung, and M. S. Cha, Combust. Flame **163**, 317 (2016).

[31] J. Prager, U. Riedel, and J. Warnatz, Proc. Combust. Inst. **31**, 1129 (2007).

[32] M. J. Papac and D. Dunn-Rankin, Combust. Theory Model. **12**, 23 (2008).

[33] T. A. Cool and P. J. Tjossem, Chem. Phys. Lett. **111**, 82 (1984).

[34] C. K. Law, *Combustion Physics* (Cambridge University Press, Cambridge, 2006).

[35] See Supplemental Material at http://link.aps.org/supplemental/10.1103/PhysRevE.97.013103 for a video of the flame electrohydrodynamic instability phenomenon.

[36] J. P. Sethna, K. Dahmen, S. Kartha, J. A. Krumhansl, B. W. Roberts, and J. D. Shore, Phys. Rev. Lett. **70**, 3347 (1993).

[37] W. Yan and J. F. Brady, Phys. Rev. E **96**, 060601 (2017).

[38] J. Kuhl, T. Seeger, L. Zigan, S. Will, and A. Leipertz, Combust. Flame **176**, 391 (2017).

[39] E. N. Volkov, V. N. Kornilov, and L. P. H. De Goey, Proc. Combust. Inst. **34**, 955 (2013).

[40] F. J. Crary, J. T. Clarke, M. K. Dougherty, P. G. Hanton, K. C. Hansen, J. T. Steinberg, B. L. Barraclough, A. J. Coates, J. C. Gérard, D. Grodent, W. S. Kurth, D. G. Mitchell, A. M. Rymer, and D. T. Young, Nature **433**, 720 (2005).

[41] J. M. Bergthorson, K. Sone, T. W. Mattner, P. E. Dimotakis, D. G. Goodwin, and D. I. Meiron, Phys. Rev. E **72**, 066307 (2005).

[42] J. Vinogradov, E. Sher, I. Rutkevich, and M. Mond, Combust. Flame **127**, 2041 (2001).

[43] J. M. Goodings, D. K. Bohme, and C.-W. Ng, Combust. Flame **36**, 45 (1979).